

Journal of Materials Chemistry A

Materials for energy and sustainability

Accepted Manuscript

This article can be cited before page numbers have been issued, to do this please use: R. Kato, K. Iwase, H. Okuyama, A. Tsurumaki, H. Kasai, K. Oka, T. Yamaguchi and T. Tomai, *J. Mater. Chem. A*, 2026, DOI: 10.1039/D6TA00970K.



This is an Accepted Manuscript, which has been through the Royal Society of Chemistry peer review process and has been accepted for publication.

Accepted Manuscripts are published online shortly after acceptance, before technical editing, formatting and proof reading. Using this free service, authors can make their results available to the community, in citable form, before we publish the edited article. We will replace this Accepted Manuscript with the edited and formatted Advance Article as soon as it is available.

You can find more information about Accepted Manuscripts in the [Information for Authors](#).

Please note that technical editing may introduce minor changes to the text and/or graphics, which may alter content. The journal's standard [Terms & Conditions](#) and the [Ethical guidelines](#) still apply. In no event shall the Royal Society of Chemistry be held responsible for any errors or omissions in this Accepted Manuscript or any consequences arising from the use of any information it contains.

ARTICLE

Size-Controlled Hydrothermal Synthesis of Crystalline High-Entropy Spinel Oxide Nanoparticles for Oxygen Evolution ElectrocatalystsRyoga Kato,^{ab} Kazuyuki Iwase,^{*b} Hiroto Okuyama,^c Akiko Tsurumaki,^{de} Hitoshi Kasai,^b Kouki Oka,^b Takeo Yamaguchi,^c and Takaaki Tomai^{ibf}Received 00th January 20xx,
Accepted 00th January 20xx

DOI: 10.1039/x0xx00000x

High-entropy oxides offer a promising platform for oxygen evolution reaction catalysis owing to their entropy-stabilized structures and flexible design of cation metal elements. However, conventional high-temperature synthesis leads to extensive particle growth and limits access to nanoscale particles with higher density of catalytic sites. Here, a subcritical hydrothermal synthesis combined with catechol-assisted growth regulation is introduced to produce high-entropy single-phase spinel oxide nanoparticles with controlled crystallite sizes down to the single-nanometer scale. The resulting reduction in particle size markedly enhances the oxygen evolution activity. A linear dependence of the oxygen evolution current density on the inverse crystallite size highlights the critical role of nanoscale structures in accelerating catalytic reactions. In-situ X-ray absorption spectroscopy reveals electronic and structural robustness of all constituent metal elements under OER conditions, with negligible shifts in oxidation state or changes in local coordination structure, which is distinct from the pronounced reconstruction typically observed in conventional oxide catalysts. When deployed in a membrane electrode assembly, our synthesized high-entropy oxide catalysts with the smallest particle size deliver 2.0 A cm⁻² at 1.96 V, demonstrating practical relevance for high-current-density electrolysis. This work establishes low-temperature hydrothermal synthesis with organic molecular regulation as a powerful and scalable route to engineer highly crystalline, compositionally homogeneous high-entropy oxide nanoparticles, offering design guidelines for next-generation oxygen evolution reaction catalysts.

Introduction

The oxygen evolution reaction (OER) is the anodic reaction in electrochemical water splitting. It plays a pivotal role in enabling the generation of green hydrogen using renewable electricity sources. However, the OER suffers from sluggish kinetics and a large overpotential, which significantly reduces the overall efficiency of water splitting.^{1, 2}

In recent years, metal oxides composed of only non-precious metal elements have drawn increasing interest for the OER catalysts due to their high activity under alkaline conditions and the ability to modulate OER activity through electronic structure and structure tuning.³⁻⁶ High-entropy oxides (HEO),

usually composed of more than five metal elements, have recently attracted significant attention as promising catalytic materials.⁷⁻⁹ This growing interest is largely due to their unique electronic structure, various types of active sites formed on the surface, and high durability.^{9, 10} These features distinguish HEOs from traditional metal oxide catalysts, and these properties make HEOs highly attractive for various catalytic reactions including OER. As OER electrocatalysts, HEOs composed of transition metals have attracted considerable attention, particularly because they exhibit efficient and stable catalytic activity in alkaline solutions.^{11-12, 13-17}

In previous research, HEOs have typically been synthesized through a high-temperature heat treatment process (~ 1000 °C).¹⁸ This synthesis process allows for the mixing of multiple metal elements at the atomic level. However, under these high-temperature conditions, the particle size tends to increase, and micro-size particles are usually formed. From the viewpoint of the catalysis, catalyst particles with small particle size are attractive due to their high surface area, a higher ratio of low-coordinated sites, which are expected to exhibit enhanced catalytic activity. Therefore, control over the particle size of HEOs is limited under high-temperature conditions during synthesis.

Supercritical and subcritical water have been widely utilized as reaction media for nanoparticle synthesis owing to their unique physicochemical properties.^{19, 20} In particular, the

^a Department of chemical engineering, Graduate school of engineering, Tohoku University, 6-6-11-604 Aramaki-aza Aoba, Aoba-ku, Sendai 980-8579, Japan.

^b Institute of Multidisciplinary Research for Advanced Materials, Tohoku University, 2-1-1 Katahira, Aoba-ku, Sendai, 980-8577, Japan

^c Laboratory for Chemistry and Life Science, Institute of Science Tokyo, R1-17, 4259 Nagatsuta-cho, Midori-ku, Yokohama, Kanagawa 226-8501, Japan

^d Department of Chemistry, Sapienza University of Rome, Piazzale Aldo Moro 5 00185, Rome Italy

^e Hydro-Eco Research Center, Sapienza University of Rome, Via A. Scarpa 16 00161, Rome Italy

^f The Frontier Research Institute for Interdisciplinary Sciences, Tohoku university, 6-3 Aramaki Aoba, Aoba-ku, Sendai, Miyagi 980-0845, Japan

[†] Footnotes relating to the title and/or authors should appear here.

Supplementary Information available: [details of any supplementary information available should be included here]. See DOI: 10.1039/x0xx00000x



ARTICLE

drastic changes in water properties near the supercritical state can promote the simultaneous precipitation of multiple metal species, which is expected to facilitate the formation of compositionally homogeneous multicomponent oxides. Previous studies, including our earlier work, have demonstrated that single-phase high-entropy oxides composed of five transition metals can be synthesized using supercritical water, even at relatively low temperatures around 400 °C.^{21, 22} Compared with supercritical water, subcritical water provides a milder reaction environment while still retaining unique properties of high-temperature and pressure water that promote metal oxide nucleation and crystallization.

In the present study, we employ a subcritical hydrothermal method for synthesizing size-controlled high-entropy oxide nanoparticles (HEO NPs). The physicochemical properties of water change drastically under high temperature and pressure, which is expected to facilitate the formation of nanoparticles with homogeneous solid solutions at lower temperatures than conventional methods. Furthermore, subcritical water can form a homogeneous phase with organic compounds, allowing organic modifiers to interact with the particle surface and suppress particle growth.¹⁵ This milder reaction environment is particularly advantageous for the present study, as it enables effective interaction between catechol and the surface of HEO nanoparticles and precursor metal ions while minimizing thermal decomposition of the organic modifier. In this study, we propose an organic-molecule-assisted subcritical hydrothermal strategy to achieve precise particle size control of HEO NPs.

Results and Discussion

The HEO NPs were synthesized using the hydrothermal method by modifying the method reported previously. Briefly, the metal-containing precursors were transferred to a Hastelloy reactor and heated at 300 °C for 60 min. Each synthesized sample was labeled with the concentration of catechol. Samples with a concentration of catechol of 0 M, 0.1 M, 0.3 M, 0.5 M were labeled HEO-0, HEO-0.1, HEO-0.3, HEO-0.5, respectively.

X-ray diffraction (XRD) patterns of the synthesized HEO NPs are presented in Figure 1. The observed peaks for all HEO NPs, including the main peak around 35°, can be indexed to a cubic spinel structure with the space group Fd-3m (No. 227) regardless of the catechol concentration. This result confirms that single-phase cubic spinel oxide structure was successfully formed without any side products. This result is particularly notable, as phase separation is often observed in multicomponent systems such as HEOs.⁷ An increase in catechol concentration leads to broadening of peaks, which will be discussed in detail later. Figure S1 shows synchrotron XRD patterns of HEO NPs. This result shows good agreement with the XRD patterns in Figure 1, and also indicates that single phase cubic spinel oxide structure was successfully formed during the syntheses.

The particle size and morphologies of the HEO NPs are directly analyzed by the transmission electron microscope (TEM) images (Figure 2). The particle size distribution obtained by the TEM images is shown in Figure S2. For HEO-0, particles

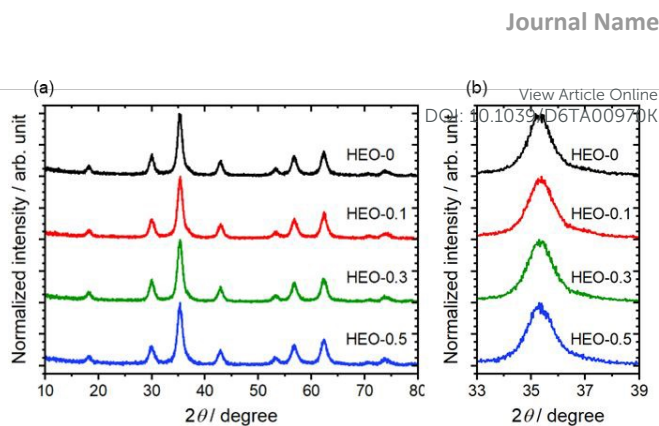


Figure 1. XRD patterns of HEO NPs with different catechol concentration. (a) Wide-angle view and (b) magnified view around the (311) peak.

with diameters approximately 20 nm were observed. However, the addition of catechol significantly reduced the particle size, with nanoparticles smaller than 15 nm obtained even at low catechol concentrations. A clear trend that increasing the catechol concentration led to progressively smaller particles was observed. Notably, the average particle diameter was approximately 5.6 nm for HEO-0.5. In addition, the particle size distribution seems to get smaller by addition of catechol during the synthesis. Figure S3 shows the comparison between crystallite size calculated from XRD pattern shown in Figure 1 using Halder-Wagner equation and the particle size obtained by TEM images against the concentration of catechol.²³ A similar trend was observed for both crystallite size and particle size, which decreased with increasing catechol concentration. For HEO-0.5, the calculated crystallite size was approximately 6 nm, further confirming the size reduction effect of catechol during synthesis.

In order to investigate whether catechol molecule modify onto the surface of HEO NPs, simultaneous differential thermal analysis (DTA) and thermogravimetric analysis (TG) were conducted. Figure S4 shows the TG and DTA curves for

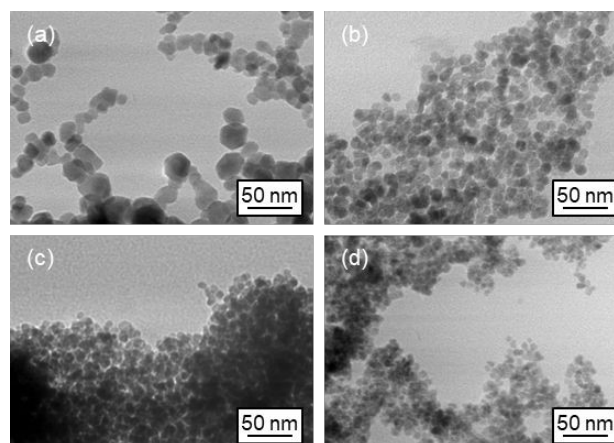


Figure 2. TEM images of HEO NPs. (a) HEO-0, (b) HEO-0.1, (c) HEO-0.3, (d) HEO-0.5. In TG curves, a slight weight loss was observed up to approximately 200 °C, which can be attributed to the removal of residual water.^{24 25} For HEO-0.5, a significant weight loss was observed above 250 °C, which was not



observed for HEO-0, accompanied by a strong exothermic peak in the DTA curve around 280–290 °C. The weight loss above 250 °C can be assignable to thermal decomposition and/or desorption of catechol. Notably, this decomposition occurs at temperatures higher than the boiling point of catechol (245 °C). This result indicates that catechol is chemically bonded to the particle surface in a stable manner.²⁶ These findings support that catechol molecules reduced the particle size likely due to the suppression of crystal growth by the surface-bound catechol.

The elemental analysis by ICP-OES was conducted for HEO NPs. The elemental ratio of the starting material and HEO NPs are summarized in Figure S5. Notably, the metal elemental ratios of HEO-0 were almost identical to those of the precursor solution, however, the ratios for HEO synthesized with catechol are different from that of precursor solution. Specifically, ratio of Mn is significantly smaller compared to the precursor solution. This result indicates that catechol molecules strongly interact with Mn species. In addition, it is plausible that catechol also forms coordination complexes with other transition-metal species except Fe, resulting in partial retention of these metal ions in the solution phase during the hydrothermal process.

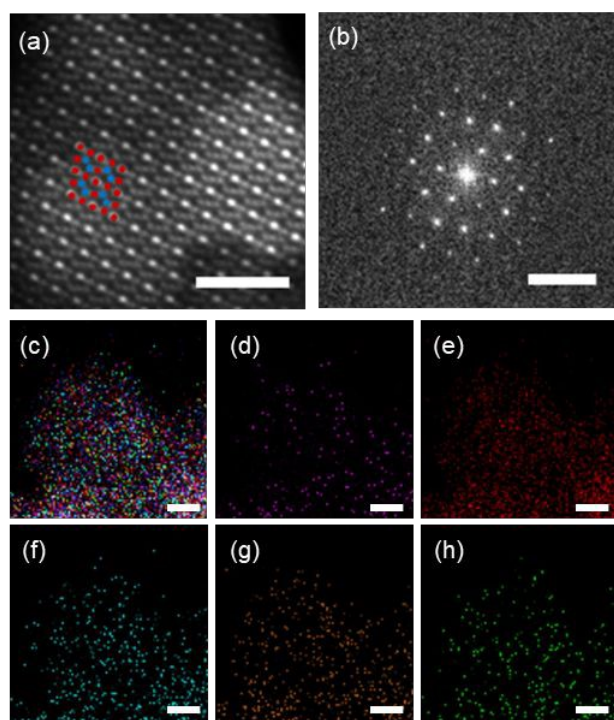


Figure 3. STEM images of HEO NPs. (a) Magnified HAADF-STEM image (zone axis: [110]). Red and blue dots correspond to 16d sites and 8a sites of the cubic spinel structure, respectively. Scale bar: 2 nm. (b) Fourier-transformed magnified HAADF-STEM image. Scale bar: 5 nm⁻¹. (c–h) EDX-mapping of HE-SOs: (c) merged image, (d) Mn, (e) Fe, (f) Co, (g) Ni, and (h) Zn. Scale bar: 2 nm.

Further detailed structure characterizations of the mixing state of the constituent elements were conducted by scanning transmission electron microscopy (STEM) technique. Figure 3 shows the HAADF-STEM images and corresponding EDX

mapping of HEO-0.5. HAADF-STEM image of zone axis [110] is shown in Figure 3a. In this image, the bright spots indicate the metal elements. The 16d and 8a sites of the cubic spinel structure marked with red and blue dots were clearly observed.²¹ The Fourier transform (FT) image of Figure 3a is shown in Figure 3b. This image provides information on the crystal structure of this region. The absence of clear unassigned diffraction spots implies that HEO-0.5 has a single-phase spinel structure. These results are well consistent with the synchrotron XRD patterns. STEM-EDX elemental mapping for the constituent metal elements (Figure 3c–h) shows that constituent elements are homogeneously distributed across the particles. These results indicate that no elemental segregation occurs during the synthesis even in a presence of catechol. These results indicate that the five metal elements are uniformly distributed across the particle. The wide range STEM-EDX mapping for HEO-0.5 (Figure S6) also revealed that large detectable phase segregation did not occur during the synthesis procedure.

Detailed analyses of the valence states and coordination environments of the metal elements were conducted using X-ray absorption spectroscopy (XAS). XAS was selected because conventional X-ray photoelectron spectroscopy (XPS) is not suitable for this system; in multicomponent oxides containing several first-row transition metals, overlapping Auger and metal 2p peaks make reliable valence analysis difficult.

The XANES spectra of the Mn, Fe, Co, Ni, and Zn K-edges for HEO-0.5 are listed in Figure 4a–e, respectively. The absorption edges of Mn, Co, Ni, and Zn exhibit absorption-edge energies

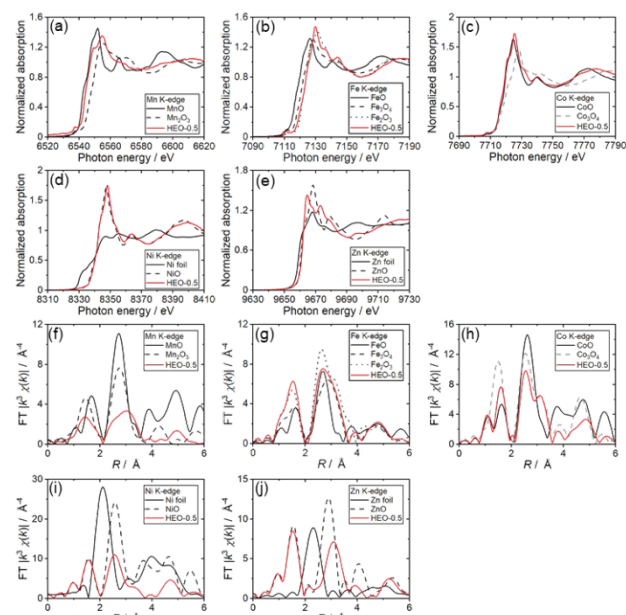


Figure 4. Metal K-edge (a–e) XANES and (f–j) FT-EXAFS of constituent metal elements of the HEO-0.5. (a, f) Mn, (b, g) Fe, (c, h) Co, (d, i) Ni, and (e, j) Zn.



similar to the corresponding metal oxides containing divalent metal ions (M(II)), whereas Fe exhibits absorption-edge energies similar to the corresponding trivalent metal ions (M(III)). These results suggest that Mn, Co, Ni and Zn exist as M(II), and Fe exists as M(III). XANES spectra of metal K-edges for HEO-0, -0.1 and 0.3 are shown in Figure S7. Although all metal K-edges for HEO-0.1 and HEO-0.3 exhibited a similar tendency to HEO-0.5, however, HEO-0 show the different absorption-edge energy for Mn K-edges, and the absorption edges are similar to Mn_2O_3 , suggesting that Mn species for HEO-0 exist as Mn(III). This result also suggests that catechol molecule largely affected on the valence for Mn species as discussed in ICP analyses, but the particle size itself doesn't affect the valence of the constituent metal elements.

The corresponding Fourier transformed extended X-ray absorption fine structure (FT-EXAFS) spectra also reveal well-defined first shell M–O (~ 1.5 Å) and second-shell M–O–M (~ 2.5 – 3.1 Å) peaks which are observed in cubic spinel structure (Figure 4f-j).²⁷ In HEO-0.5, Ni shows clear second-shell features around ~ 2.6 Å, consistent with their occupancy at octahedral (16d) sites, while Zn shows clear second-shell features around ~ 3.1 Å, consistent with their occupancy at tetrahedral (8a) sites. For Mn, Fe, and Co K-edges, the spectra displayed spectral features with distributions over both tetrahedral (8a) and octahedral (16d) sites, suggesting that those metal elements occupies both 8a and 16d sites. FT-EXAFS spectra of metal K-edges for HEO-0, -0.1 and 0.3 are shown in Figure S8. The tendency is similar to XANES spectra of those samples. Although the shape of the FT-EXAFS for HEO-0.1 and HEO-0.3 exhibited a similar tendency to HEO-0.5 for all metal elements. However, HEO-0 for Mn K-edges showed different peak position. The second-shell M–O–M spectra for HEO-0 showed the single peaks at shorter region around 2.6 Å, suggesting that Mn occupies octahedral sites. These results indicate that catechol affects not only the Mn valence state but also its local coordination environment. This change possibly the reason of the reduced Mn incorporation observed by ICP-OES, suggesting that catechol selectively modifies the Mn incorporation pathway during HEO formation.

To evaluate the OER activity, cyclic voltammetry (CV) was recorded in O_2 -saturated 1 M KOH aqueous solution (Figure 5a). All samples exhibited a clear increase in anodic current assignable to OER approximately from 1.5 ~ 1.55 V vs. reversible hydrogen electrode (RHE). A comparison among the samples clearly shows that the anodic current increases with increasing catechol concentration during the synthesis, with HEO-0.5 exhibiting the highest OER current. The current density at 1.65 V vs. RHE reached approximately 190 mA cm^{-2} for HEO-0.5. The overpotentials determined as the potential reaching 10 mA cm^{-2} for these catalysts range between 342 and 327 mV, which are comparable value as the reported NiFe- and CoFe-based spinel oxide reported so far as summarized in Table S1.²⁸⁻³² HEO synthesized without catechol shows the highest overpotential, implying that catechol addition is effective for enhancing OER activity.

Figure 5b presents the Tafel plots obtained from the chronoamperometric OER measurements. The Tafel slope value is summarized in Table S1. All HEO NPs showed linear region in

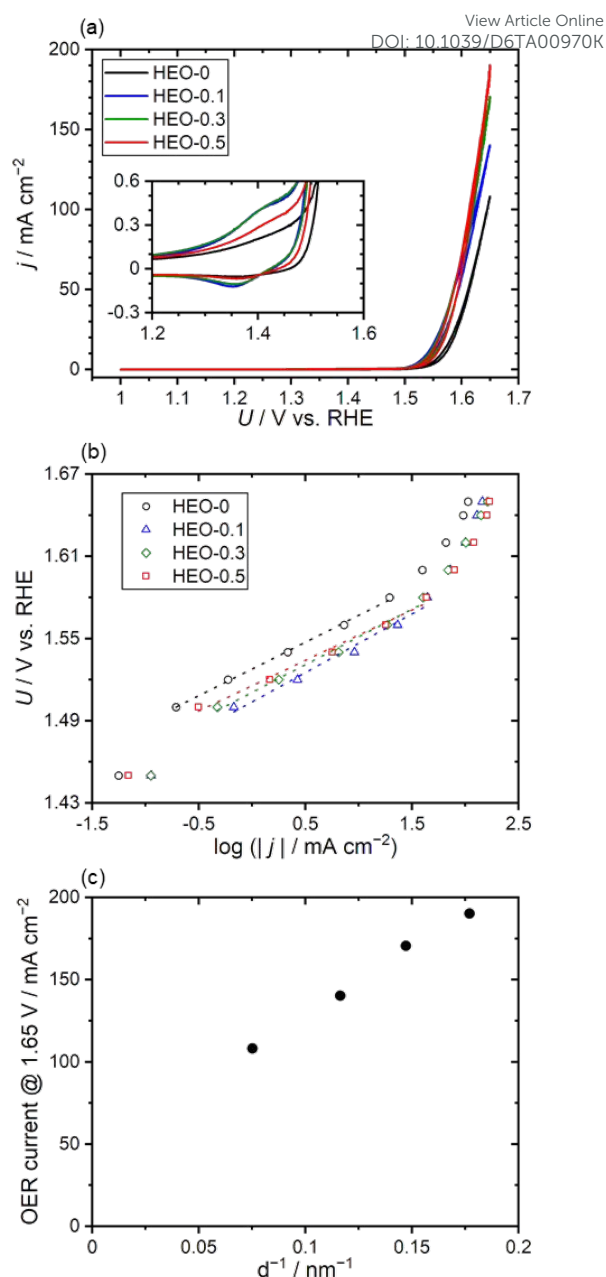


Figure 5. OER activity of HEO NPs in this study. (a) Cyclic voltammograms of HEO NP and (b) Tafel plot of HEO NPs obtained by the chronoamperometric measurement. (c) Summary of the current density at 1.65 V vs. RHE against inverse of crystallite size.

the range of approximately 1.50~1.56 V and The Tafel slope value of HEO-0 was approximately 37.7 mV dec^{-1} . This value is superior to the typical NiFe- and CoFe-based spinel oxide as summarized in Table S1, indicating better OER kinetics of the synthesized HEO catalysts. This Tafel slope value indicates that the rate-determining step is possibly step for the formation of M–O species from M–OH species or M–OO- species from M–OOH species.³³ For HEO NPs synthesized using catechol, as the catechol concentration increased, the Tafel slope value slightly decreased, reaching approximately 34.0 mV dec^{-1} for HEO-0.5. Although this change does not indicate a substantial change in



the overall reaction mechanism, it implies subtle modifications to the surface electronic structure and the adsorption energetics of reaction intermediates. Another possible reason is that the increase in low-coordination surface sites and lattice distortion accompanying the reduction in particle size may influence the adsorption energies of OER intermediates (*OH, *O, *OOH), thereby affecting the reaction kinetics.^{34, 35}

The enhancement of OER activity could also be attributed by increasing catechol concentration due to their reduced particle size upon catechol addition. Therefore, to clarify the correlation between OER activity and particle size, the current density at 1.65 V vs. RHE was plotted as a function of the inverse crystallite size ($1/d$), as shown in Figure 5c. A clear linear relationship was observed against the inverse crystallite size, demonstrating that the reduction in particle size directly contributes to the enhancement of OER current density. This trend suggests that the increased number of accessible active sites, together with the higher density of low-coordination atoms and surface lattice distortion, plays a significant role in accelerating the OER. In particular, previous studies have reported that surface strain originating from the configurational disorder of constituent elements can act as active sites of the reaction, especially in nanoscale materials in high-entropy oxides.³⁶ The present results of our HEO catalysts indicate that not only the metal mixing entropy effect suggested by the previous study but the particle size showed positive effect on the catalytic activity. Overall, these findings demonstrate that particle-size control through organic molecule modification not only tunes the geometric structure of the catalyst but also leads to substantial improvements in electrocatalytic activity.

To investigate whether the electrochemical surface area (ECSA) supports the observed particle-size-dependent OER activity, the double-layer capacitance (C_{dl}) was estimated from CVs recorded in the non-faradaic region at different scan rates (Figure S9). In this study, carbon nanotubes (CNTs) were added during the preparation of HEO-modified electrodes (see Experimental Section for details). However, CNT-free HEO electrodes were specifically employed for the C_{dl} measurements to exclude the contribution of CNT capacitance. The estimated C_{dl} did not show a monotonic increase with decreasing particle size, nor did it correlate with the trend in OER activity. This result indicates that CV-derived C_{dl} is not a reliable descriptor of the ECSA of HEO-modified electrodes under the present electrode configuration likely due to its sensitivity to film conductivity, interparticle contact, and electrolyte accessibility. Since the capacitance in CNT-containing electrodes is dominated by CNTs, the C_{dl} -derived ECSA was not used as a quantitative measure of active site density in this study.

To investigate the redox behavior and local coordination structures changes of the constituent elements of the redox region (around 1.4 V as shown in Figure 5a) and around the starting potential of OER, *in situ* XAFS measurements were conducted for HEO with the highest OER activity, HEO-0.5 (Figure 6). Previous studies have suggested that nanoparticles with particle sizes below approximately 20 nm possess a higher ratio of surface metal atoms, making it possible to analyze redox and structural changes.³⁷⁻³⁹

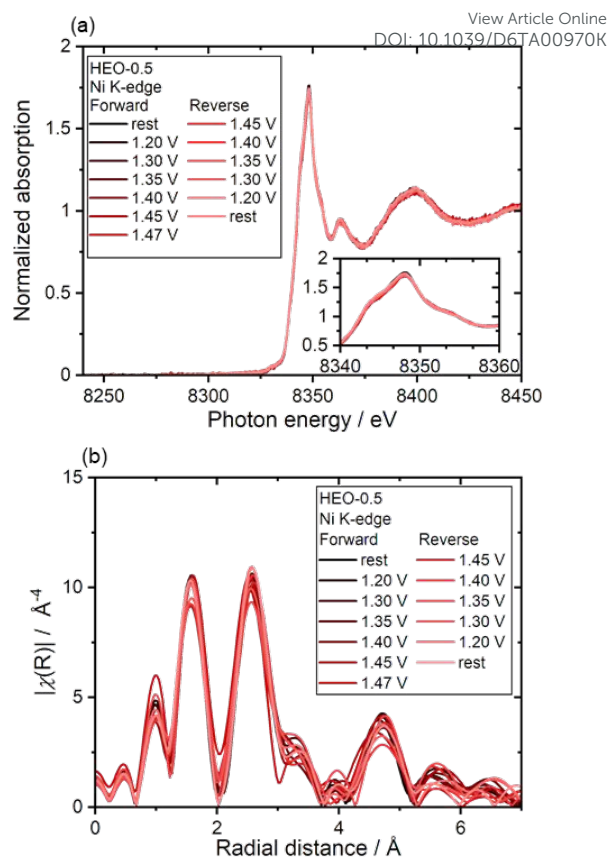


Figure 6. In-situ (a) XANES and (b) FT-EXAFS spectra of the Ni K-edge for the HEO-0.5 in the redox region. The potential sweep is initially from 1.2 V to 1.47 V as the forward scan and then returned to 1.2 V during the reverse scan.

Figures 6a, b show the in-situ XANES and FT-EXAFS spectra for Ni K-edge, respectively. For XANES spectra, no significant energy shifts or noticeable changes in white-line intensity were observed within the redox potential window of 1.2–1.47 V vs. RHE. This behavior contrasts with the pronounced structural changes previously observed for monometallic Ni-based oxides and is instead consistent with the behavior reported for HEOs with particle sizes around 20 nm composed of Mn, Fe, Co, Ni and Zn.³⁷ This result realized the moderate oxidation and structural stability of Ni species. In addition, no obvious changes for the M-O peaks or M-O-M peaks were observed for in-situ FT-EXAFS (Figure 6b). These results also indicate that HEOs possess structural stability against potential changes within the potential region examined in this study. In-situ XANES and FT-EXAFS spectra for other elements are summarized in Figure S10 and S11, respectively. For all metal species, no significant energy shifts or noticeable changes in white-line intensity were observed within the redox potential window of 1.2–1.47 V in XANES spectra and FT-EXAFS. These results also suggest that all constituent elements in HEO-0.5 show structural stability in the potential window in this study.

It is well known that transition-metal oxides, including Ni-, Co-, and Fe-containing spinel oxides, often undergo structural reconstruction during the OER, involving phase transitions (e.g.,



from spinel oxides to layered metal oxyhydroxide structure) and changes in oxidation state.^{39, 40} These reconstruction processes are widely considered to play a key role in enhancing the OER activity of transition-metal oxides.⁴¹ In contrast to conventional spinel-type transition metal oxides, which typically undergo irreversible surface reconstruction into hydroxide or oxyhydroxide phases under OER conditions,^{42, 43} HEO-0.5 maintains a relatively stable multi-cation local structure even under applied potential conditions, as evidenced by in-situ XAS analysis. This relatively higher structural stability, while not excluding subtle structural modifications at the outermost surface, can be rationalized by the synergistic effects of entropy-driven stabilization and the high crystallinity of the nanoparticles. First, the homogeneous mixing of multiple metal cations gives rise to a higher configurational entropy, which can contribute to stabilization of the multication spinel framework. This stabilization may mitigate cation segregation and extensive structural reconstruction, both of which are closely related to degradation in conventional spinel oxide catalysts.^{43, 44} Second, unlike typical amorphous or polycrystalline catalysts, where phase transformations often initiate at grain boundaries or defect sites,⁴⁵ the high crystallinity of the single-nanometer scale HEO-0.5 nanoparticles could provide a robust framework that resists extensive self-oxidation and bulk phase transformation.⁴⁵ The low density of extended defects in highly crystalline HEO-0.5 may also inhibit the nucleation of oxyhydroxide phases. Thus, while subtle surface reconstruction or trace metal dissolution cannot be excluded, the *in situ* XAS results indicate that HEO-0.5 largely preserves its multication spinel framework under the examined oxidative conditions.

To quantitatively evaluate the changes in oxidation state for each metal species, the mid-point energies (half-height positions of the absorption edge) of the in-situ XANES spectra were plotted as a function of the applied potential (Figure 7).³⁸ For Ni, a reversible shift toward higher energies was observed, particularly in the high-potential region above 1.45 V. In contrast, Mn, Fe and Zn exhibited no apparent potential-dependent energy shifts within the range of 1.2–1.47 V. The Co K-edge appears to slightly shift to higher energy region under higher potential region although the noise by the fluctuation was observed. This indicates that, over the potential window where the redox process proceeds as shown in Figure 5a, the

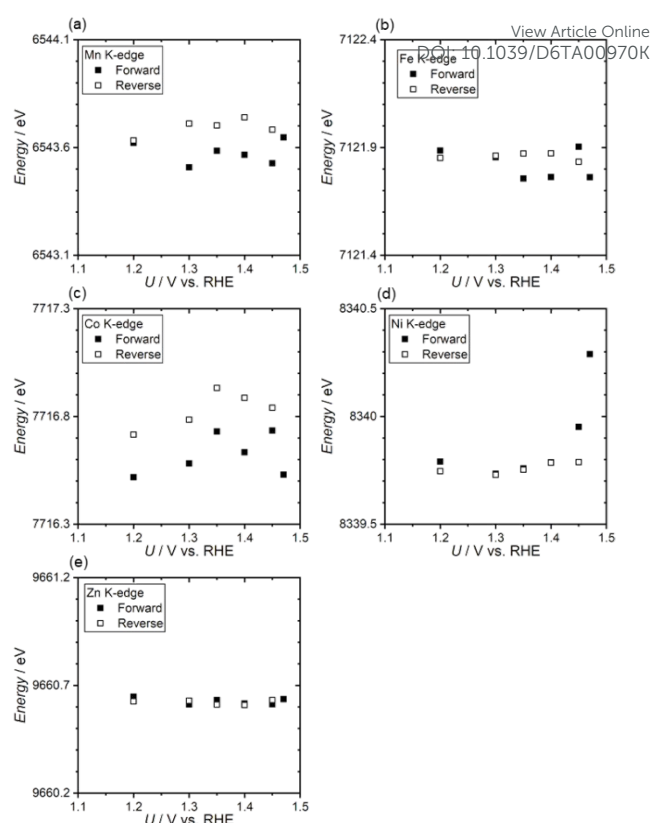


Figure 7. Mid-point plot of the in-situ XANES spectra for metal K-edge. (a) Mn, (b) Fe, (c) Co, (d) Ni, and (e) Zn.

average oxidation states of these metals, Mn, Fe and Zn, remain essentially unchanged or undergo only minimal changes. On the other hand, Co and Ni show moderate redox activity during the potential applications. These observations are consistent with the absence of obvious potential-dependent features in the full XANES spectra shown in Figure 6, S9 and S10, further supporting that the constituent elements in HEO-0.5 remained more stable under reaction conditions. This suggests that entropy-driven stabilization by multi-metal cation mixing and the robust spinel framework of the high-entropy oxide suppress local structural changes, leading to enhanced electronic stability relative to traditional oxide catalysts.²⁸⁻³²

For further investigating the impact of the synthesis process against morphology and OER activity, HEO were synthesized under hydrothermal conditions at 200 °C with and without catechol, which are labelled as HT-HEO-0.5 and HT-HEO-0, respectively. For the XRD pattern of both catalysts (Figure S12), clear peaks assignable to single phase spinel structure were observed as observed for HEO-0~HEO-0.5, although main peaks around 36° were broadened for HT-HEO-0.5. TEM images also show that nanoscale particles were obtained (Figure S13). However, amorphous-like regions appearing in brighter contrast were also observed with darker contrast particles which could be originated more crystallized particles. OER activities were evaluated with similar manners for HEO catalysts (Figure S14). Clear OER current is observed for both catalysts (Figure S14a). Notably, the overpotential for HT-



HEO-0.5 shows the smallest value among the samples synthesized in this study. However, the Tafel plots for HT-HEO-0.5 shows larger slope among the samples synthesized in this study (Figure S14b). The Tafel slope value for HT-HEO-0.5 shows the larger value as summarized in Table S1. The OER current of the samples against the inverse of crystalline size was plotted in Figure S14c. Interestingly, the OER current at 1.65 V shows for HT-HEO catalysts shows the same tendency as the HEO catalysts, catalysts with lower crystalline size shows higher OER current. However, although the crystalline sizes are similar to HEO catalysts, the OER current at 1.65 V shows for HT-HEO shows the smaller value. This result indicates that synthesis process can affect the OER activity. We hypothesize that the superior OER activity for HEO catalysts is derived from higher crystallinity due to the higher temperature during the synthesis. Further study for investigating the relation between the physicochemical properties, such as crystallinity and size, and OER activity is ongoing in our laboratory.

To evaluate the practical applicability of the synthesized HEO, we integrated the most OER-active composition, HEO-0.5, into a MEA and tested its performance under device-relevant conditions. Anion exchange membrane water electrolysis (AEMWE) cells were assembled using HEO-0.5 as the anodic OER catalyst and PtRu/C as the cathode, operated with a commercially available thin anion-exchange membrane and 1.0 M KOH at 80 °C. The anodic catalyst layer composition was systematically tuned by varying the mass ratio of HEO-0.5 to metallic Ni while keeping the total loading weight constant. Figure S15a shows the polarization curves obtained from these MEAs. The dependence of MEA performance on the Ni:HEO ratio highlights the importance of balancing electronic conductivity and active site density in the anodic catalyst layer. At a Ni:HEO ratio of 5:5, the polarization curve was shifted to lower cell voltages across the entire current density range compared with 3:7 and 7:3, indicating that this composition provided the most efficient compromise between a well-percolated conductive network and a high density of active HEO-0.5 sites. When the Ni fraction was reduced to 30 wt% (Ni:HEO = 3:7), the cell voltage slightly increased, which attributed to higher ohmic and contact resistances associated with an insufficiently connected Ni network. Conversely, when the Ni fraction is increased to 70 wt% (Ni:HEO = 7:3), the performance deteriorates more significantly, especially in the high-current-density region, indicating that the loss of active HEO-0.5 per geometric area outweighs the benefit of enhanced conductivity. These trends indicate that performance is governed by the balance between electronic conductivity and active-site density, and that an intermediate Ni content maximizes the effective utilization of both the conductive additive and the catalyst.

Figure 8 shows the polarization curve obtained from the MEA optimized Ni:HEO-0.5 ratio (5:5). The cell with an optimized Ni:HEO ratio of 5:5 exhibited a current density of 1.0 A cm⁻² at 1.83 V and reached 4.0 A cm⁻² at 2.19 V under differential-pressure-free conditions. These results demonstrate that the fully non-noble HEO-0.5 catalyst can drive the OER in a device-relevant configuration, achieving high

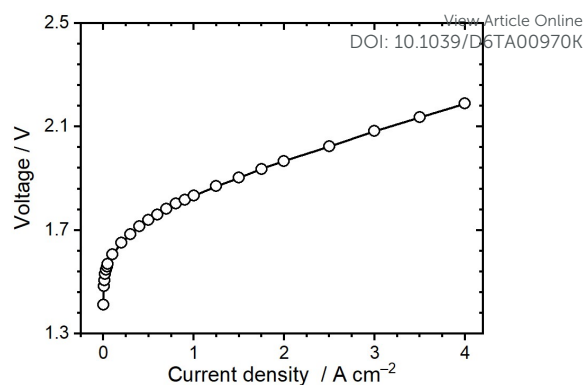


Figure 8. Polarization curve of AEMWE cell using HEO-0.5/Ni anodes in 1.0 M KOH at 80 °C. In this measurement, the HEO-0.5:Ni ratio is 5:5. For the detail of the optimization of the catalyst: Ni ratio, see supporting Figure S15.

current densities at low cell voltages around 1.8–2.2 V. When compared with recently reported non-noble AEMWE cells operated at 80 °C in 1.0 M KOH, which typically require 1.65–2.03 V to deliver 1.0 A cm⁻², the present HEO-0.5 MEA lies in the upper tier of performance (Table S2, Figure S16),^{46–53} despite the relatively modest catalyst loading and the absence of advanced electrode structuring. This device-level activity is in good agreement with the high intrinsic OER activity of HEO-0.5 evidenced by half-cell measurements (Table S2, Figure S16).

To gain further insight into the origin of these MEA-level trends, electrochemical impedance spectroscopy (EIS) was conducted under operating conditions (Figure S15b, see Experimental Section for experimental detail). In all cases, the high-frequency intercept of the Nyquist plots was nearly identical, indicating that the bulk ohmic resistance of the membrane and cell hardware was essentially unchanged by the Ni:HEO ratio. In contrast, the diameter of the main semicircle, associated with the charge-transfer resistance (R_{ct}), depended strongly on the anode composition: R_{ct} remained small for Ni:HEO = 3:7 and 5:5 but increased markedly for 7:3, in line with the larger voltage losses observed for the Ni-rich electrode at high current densities. Furthermore, EIS-based analysis of the cell voltage allowed separation of the anodic and cathodic contributions at each electrode (Figure S15c,d). The cathodic overpotential was almost identical for all cells, as expected from the identical cathode configuration, whereas the anodic overpotential varied with the Ni:HEO ratio and reached a minimum at 5:5. This composition-dependent trend in anodic overpotential closely matches the polarization behavior in Figure 8, with the lowest anodic losses coinciding with the best MEA performance at Ni:HEO = 5:5.

Overall, the combination of polarization and EIS analyses demonstrates that the size-controlled HEO-0.5 catalyst, when combined with an optimally balanced Ni content in the anode, delivers high MEA performance using only non-noble metals. Because the catalyst is entirely non-noble, increasing its loading and refining the electrode architecture should further enhance MEA performance. Since the choice of metal cations and cell



configuration can influence both the catalytic activity and the stability of the catalyst¹⁴ and MEA cell operation, further studies aimed at enhancing stability as well as OER activity represent promising future directions.

Conclusions

In conclusion, in this study, we have demonstrated a subcritical hydrothermal synthesis strategy combined with surface organic modification as an effective route to synthesize size-controlled multi-metal HEO as OER catalysts. This approach enabled the synthesis of single-phase, highly crystalline cubic spinel HEO nanoparticles with tunable particle sizes down to the single-nanometer scale, which is difficult to achieve via conventional high-temperature annealing synthesis protocol. Systematic particle size reduction induced by catechol addition resulted in a pronounced enhancement of OER activity. The optimized HEO-0.5 catalyst delivered high current densities and exhibited a clear linear correlation between the OER current density and the inverse crystallite size, highlighting the critical role of nanoscale structural control in maximizing accessible active sites. Beyond activity enhancement, in-situ XAS analysis revealed that the multi-cation local structure of HEO-0.5 remains relatively stable under potential applied conditions, showing minimal changes in oxidation state and coordination environment. This behavior contrasts sharply with the extensive surface reconstruction typically observed in conventional oxide catalysts and can be attributed to the synergistic effects of entropy-driven structural stabilization and high crystallinity enabled by the subcritical hydrothermal synthesis process. Furthermore, the practical relevance of this material design was demonstrated by MEA measurements, where the HEO-0.5 catalyst achieved high current densities at low cell voltages. Taken together, this work establishes subcritical hydrothermal synthesis with organic molecular regulation as a powerful and scalable platform for designing durable, high-performance HEO catalysts, providing valuable guidelines for OER catalysts in practical water electrolysis systems.

Experimental Section

Material synthesis

HEO NPs were synthesized via subcritical hydrothermal processing. A mixture of 0.111 mmol manganese (II) acetate tetrahydrate (Wako, Guaranteed Reagent grade, 99.9%), 0.222 mmol iron (II) acetate (Sigma Aldrich, 99.99%), 0.056 mmol cobalt (II) acetate tetrahydrate (Wako, Guaranteed Reagent grade, >99.0%), 0.056 mmol nickel (II) acetate tetrahydrate (Kanto Chemical, 98.0%), and 0.056 mmol zinc (II) acetate dihydrate (Wako, Guaranteed Reagent grade, >99.9%) was dissolved in 5 mL of ultrapure water (Milli-Q EQ 7000, 18.2 MΩ cm). The resulting solution, along with a predetermined amount of catechol (Wako, Guaranteed Reagent grade), was sealed in a 10 mL Hastelloy tube reactor. The reactor was heated at 300 °C for 60 minutes, and after cooling, the contents were transferred

to a centrifuge tube. The product was washed several times with ultrapure water, and unreacted precursors were removed by repeated centrifugation. The collected particles were then redispersed in water and freeze-dried to obtain the final powder samples.

Physical Characterizations

The crystal structure of the synthesized HEO NPs was characterized by powder X-ray diffraction (XRD) using a SmartLab 9MTP diffractometer (Rigaku) with Cu-K α radiation ($\lambda = 1.5418 \text{ \AA}$). Diffraction patterns were recorded over a 2θ range of 10° to 80° at a scan rate of $3.00^\circ \text{ min}^{-1}$. The step size was set to 0.02° , with an accelerating voltage of 45 kV and a tube current of 200 mA. The primary particles of the synthesized HEO NPs were examined using transmission electron microscopy (TEM, HITACHI H-7650) operated at an accelerating voltage of 100 kV and a filament current of 20 mA.

The amount of organic modifier bound to the product was evaluated by thermogravimetry differential thermal analysis (TG-DTA, Thermo plus EvoII (Rigaku)). The sample was heated from room temperature to 800 °C at a rate of $10^\circ \text{ C min}^{-1}$ under a flow of pure air at 100 mL min^{-1} . Prior to measurement, the samples were preheated at 60 °C for at least one hour to remove moisture contained within the particles. The elemental ratio of HEO NPs was analyzed by inductively coupled plasma atomic emission spectroscopy (ICP-AES) using SPECTRO ARCOS (SPECTRO Analytical Instruments, Germany). Scanning transmission electron microscopy (STEM) observations were performed using a Titan3 60–300 Double Corrector microscope (FEI Company) equipped with a Super-X system operated at 200 kV. X-ray absorption spectroscopy (XAS) measurements were carried out at the BL01B1 and BL14B2 beamline of SPring-8 (Japan Synchrotron Radiation Research Institute (JASRI)). A Si(111) double-crystal monochromator was employed for energy selection. The ex-situ XAS measurements were performed in transmission mode, while the in-situ measurements were conducted in fluorescence mode using a 19-element solid-state detector. The obtained data were analyzed using ATHENA software.⁵⁴ The energy levels were calibrated by setting the first peak maximum in the Cu foil spectrum equal to 8980.3 eV during the measurements.

Electrochemical measurements

Electrochemical measurements were conducted in a custom-built PTFE electrochemical cell containing 70 mL of 1 M potassium hydroxide (KOH) aqueous solutions as the electrolyte. During measurements, the electrolyte was continuously saturated with oxygen by bubbling O₂ gas through the solution. A three-electrode setup was employed, consisting of the catalyst-modified glassy carbon working electrode, a Hg/HgO reference electrode, and a graphite rod as the counter electrode, respectively. The working electrodes were prepared by drop-casting a catalyst ink onto a glassy carbon electrode, which was polished using an alumina slurry prior to use. The catalyst ink was prepared by dispersing 3 mg of the synthesized catalyst and 2 mg of oxidized carbon nanotubes (Sigma Aldrich) in a mixture of 40 μL Nafion solution (5 wt%, Sigma), 200 μL



isopropanol (Wako), and 400 μL ultrapure water. The suspension was first vortexed and then sonicated for 20 minutes to achieve a homogeneous dispersion. A volume of 7.5 μL of the ink was drop-cast onto a 5 mm-diameter glassy carbon electrode and dried at room temperature. The working electrode was rotated at 900 rpm using a rotating electrode system (Pine Research Instrumentation). All electrochemical measurements were performed using a potentiostat (SP-150e, Bio-Logic).

Preparation of membrane electrode assembly

The water electrolysis performance of the synthesized catalysts in this study was also investigated by the membrane electrode assembly (MEA) following the reported method.^{55,56} Pt₃₂Ru₁₆/C (Tanaka Precious Metal Technologies) was used as the cathode catalyst in the MEA. PiperION-A (13.3 mg, Versogen) was dissolved in a mixed solvent consisting of ethanol (3.5 mL) and deionized water (1.5 mL), and the solution was stirred overnight at 20 °C. Subsequently, 40 mg of Pt₃₂Ru₁₆/C was added to the ionomer solution and thoroughly mixed in a planetary ball mill (Pulverisette 6, Fritsch) for 1 h at 150 rpm using 5 mm ZrO₂ balls. The resulting catalyst ink was sprayed onto a PiperION anion-exchange membrane (20 μm thickness, Versogen) using a spray coater (Nordson K.K.) to form a cathode catalyst layer with a geometric area of 1 cm² and a Pt loading of 0.3 mgPt cm⁻².

To prepare anode catalyst ink, a total of 40 mg of a physical mixture of HEO-0.5 and Ni particles (Aldrich, <100 nm) was combined with PiperION-A (13.3 mg), deionized water (1.5 mL), and ethanol (3.5 mL). The mass ratio of Ni to HEO was adjusted as described in the main text, while keeping the total mass of Ni and HEO constant at 40 mg. The suspension was mixed in a planetary ball mill under the same conditions as for the cathode ink (1 h, 150 rpm, 5 mm ZrO₂ balls), and then sprayed onto the opposite side of the PiperION membrane to form the anode catalyst layer. The anode loading was controlled so that the combined mass of Ni and HEO was 1.2 mg cm⁻². A specially designed electrolyzer cell hardware (Chemix, Japan) was used for all water electrolysis tests, and the MEA was sealed between the bipolar plates with gaskets of appropriate thickness prior to measurements.

Water electrolysis test

A 1 M KOH solution was circulated through the electrolyzer at a flow rate of 5 mL min⁻¹ overnight to activate the membrane and ionomer by exchanging Cl⁻ with OH⁻. Electrochemical impedance spectroscopy (EIS) was monitored at a cell voltage of 1.5 V using an impedance analyzer (Solartron 1260) coupled with an electrochemical interface (Solartron 1287) until stable spectra were obtained. The cell temperature was then increased to 80 °C. To maintain the operating temperature, KOH solutions preheated to 80 °C were supplied to the anode and cathode through heated tubing. After stable impedance spectra were confirmed at 80 °C, the MEA was conditioned by applying a current density of 0.2 A cm⁻² for 20 min. Polarization curves were then recorded to evaluate the water electrolysis performance. During all measurements, the alkaline electrolyte was continuously circulated on both the anode and cathode

sides. Electrolysis tests were carried out using a charge-discharge system (Hokuto Denko Co., Ltd.).

Electrode-resolved EIS measurements in water electrolyzers were performed using a dual-reference-electrode electrolyzer cell based on the design reported by Nagasawa et al.⁵⁷ The cell allows reference electrodes to be inserted on both the anode and cathode sides of the membrane, enabling separation of the local anodic and cathodic potential responses. Before the measurement, the reference-electrode compartments were filled with 1 M KOH and allowed to stabilize for approximately 20 min. Mini-HydroFlex reference electrodes were then inserted into both sides of the cell. EIS spectra were recorded using a Solartron 1260 impedance analyzer coupled with a Solartron 1287 electrochemical interface. The anodic and cathodic impedance contributions were evaluated from the AC potential responses between each electrode and the corresponding nearby reference electrode.

Author contributions

R.K. performed synthesis, structural analysis, electrochemical measurements, participated in data analysis, and contributed to the initial draft of the manuscript. K.I. conceived and designed the study, supervised the project, analysed the data, and wrote the initial draft of the manuscript. A.T., K.O., and H.K. conducted synchrotron XRD measurements at the NanoTerasu facility. H.O. and T.Y. provided discussion on the interpretation of OER activity, performed the MEA tests, contributed to data interpretation, and wrote the MEA-related sections of the manuscript. T.T. contributed to experimental planning and provided project supervision. All authors discussed the results and contributed to the final version of the manuscript.

Conflicts of interest

The authors declare no conflict of interest.

Data availability

The data that support the findings of this study are available from the corresponding author upon reasonable request.

Acknowledgements

This work was supported by “Crossover Alliance to Create the Future with People, Intelligence and Materials” from MEXT, Japan. K.I. acknowledges financial support by the JSPS KAKENHI Grant (22H02175, 23KK0103), the JST PRESTO program (JPMJPR2371), and the Kato Foundation for Promotion of Science (KJ-3305), Nippon Sheet Glass Foundation for Materials Science and Engineering, JGC-S Scholarship foundation (No. 2301) and Iwatani Naoji Foundation.



This work was also supported by Material Solutions Center (MaSC), Tohoku University and Central Analytical Facility, IMRAM, Tohoku University, Japan. Synchrotron radiation experiments were performed using the BL01B1 and BL14B2 beamline of SPring-8 (Proposal Nos. 2025B1740, 2025A1811, 2024B1682, 2024B209, 2024A1587, 2023B1670, 2023B2081). We also acknowledge Dr. Y. Hayasaka in Tohoku for the HRTEM observation. The authors also thank NanoTerasu Synchrotron Light Source, the Tohoku University NanoTerasu International Co-creation Utilization Promotion Support System to access their synchrotron facility, within the research collaboration entitled "Post-mortem XPS and in-situ XRD analyses of cathode-electrolyte interphase stabilized by ionic liquids" The authors acknowledge Prof. Yuuki Sugawara in Institute of Science Tokyo for his fruitful discussion.

References

1. Y. Matsumoto and E. Sato, *Mater. Chem. Phys.*, 1986, **14**, 397-426.
2. Y. Sugawara, K. Iwase, R. Iimura, T. Yabu, A. Nasu, M. Matsui, I. Honma, T. Yamaguchi and H. Kobayashi, *ACS Appl. Mater. Interfaces*, 2025, **17**, 22487-22497.
3. Y. Yan, B. Y. Xia, B. Zhao and X. Wang, *J. Mater. Chem. A*, 2016, **4**, 17587-17603.
4. D. U. Lee, P. Xu, Z. P. Cano, A. G. Kashkooli, M. G. Park and Z. Chen, *J. Mater. Chem. A*, 2016, **4**, 7107-7134.
5. T. Katsumata, S. Kobata, Y. Watase, R. Aso, S. Yagi, Y. Kimura, K. Amezawa and T. Nakamura, *ACS Appl. Nano Mater.*, 2025, **8**, 21215-21223.
6. Y. Sugawara and T. Yamaguchi, *Chem. Rec.*, 2025, **25**, e202400246.
7. M.-H. Tsai and J.-W. Yeh, *Mater. Res. Lett.*, 2014, **2**, 107-123.
8. Z. Shi, L. Wang, Y. Huang, X. Y. Kong and L. Ye, *Mater. Chem. Front.*, 2024, **8**, 179-191.
9. Y. Sun and S. Dai, *Sci. Adv.*, 2021, **7**.
10. K. Mori, N. Hashimoto, N. Kamiuchi, H. Yoshida, H. Kobayashi and H. Yamashita, *Nat. Commun.*, 2021, **12**, 3884.
11. M. Vedanarayanan, C. Pitchai and C.-M. Chen, *J. Mater. Chem. A*, 2025, **13**, 18040-18061.
12. X. Zhang, X. Wang and X. Lv, *ChemSusChem*, 2025, **18**, e202401663.
13. J. Wang, J. Zhang, H. Yu, L. Chen, H. Jiang and C. Li, *ACS Mater. Lett.*, 2024, **6**, 1739-1745.
14. M. Rafique, T. Yao, S. Ma, Y. Xu, L. Li, J. Han, Q. Fu, W. Li, Z. Yuan, K. Wang and B. Song, *Adv. Funct. Mater.*, 2025, **36**.
15. Z. Sun, Y. Zhao, C. Sun, Q. Ni, C. Wang and H. Jin, *Chem. Eng. J.*, 2022, **431**.
16. Y. Wang, H. Liu, J. Chen, K. Han, T. Xia, H. Yang, X. Yuan and Y. Zhao, *J. Power Sources*, 2025, **655**.
17. H. Liu, Y. Wang, J. Chen, X. Yi, H. Yang, X. Yuan and Y. Zhao, *J. Power Sources*, 2025, **632**.
18. Z. Lun, B. Ouyang, D. H. Kwon, Y. Ha, E. E. Foley, T. Y. Huang, Z. Cai, H. Kim, M. Balasubramanian, Y. Sun, J. Huang, Y. Tian, H. Kim, B. D. McCloskey, W. Yang, R. J. Clement, H. Ji and G. Ceder, *Nat. Mater.*, 2021, **20**, 214-221.
19. T. Adschiri, S. Takami, M. Umetsu, S. Ohara, T. Naka, K. Minami, D. Hojo, T. Togashi, T. Arita, M. Taguchi, M. Itoh, N. Aoki, G. Seong, T. Tomai and A. Yoko, *Bull. Chem. Soc. Jpn.*, 2023, **96**, 133-147. DOI: 10.1039/D6TA00970K
20. A. Yoko, T. Kamonvarapitak, G. Seong, T. Tomai and T. Adschiri, *ChemNanoMat*, 2022, **8**.
21. K. Iwase and I. Honma, *ACS Appl. Energy Mater.*, 2022, **5**, 9292-9296.
22. S. Hanabata, K. Kusada, T. Yamamoto, T. Toriyama, S. Matsumura, S. Kawaguchi, Y. Kubota, Y. Nishida, M. Haneda and H. Kitagawa, *J. Am. Chem. Soc.*, 2024, **146**, 181-186.
23. A. Yoko, H. Naito, G. Seong, T. Tomai and T. Adschiri, *J. Phys. Chem. C*, 2021, **125**, 19489-19496.
24. J. J. Calvin, P. F. Rosen, N. L. Ross, A. Navrotsky and B. F. Woodfield, *J. Mater. Res.*, 2019, **34**, 416-427.
25. F. Kunc, M. Gallerneault, O. Kodra, A. Brinkmann, G. P. Lopinski and L. J. Johnston, *Anal. Bioanal. Chem.*, 2022, **414**, 4409-4425.
26. Y. Omura, A. Yoko, G. Seong, T. Tomai and T. Adschiri, *CrystEngComm*, 2021, **23**, 5353-5361.
27. M. H. Nilsen, C. Nordhei, A. L. Ramstad, D. G. Nicholson, M. Poliakoff and A. Cabañas, *J. Phys. Chem. C*, 2007, **111**, 6252-6262.
28. H. Zhong, T. Liu, S. Zhang, D. Li, P. Tang, N. Alonso-Vante and Y. Feng, *J. Energy Chem.*, 2019, **33**, 130-137.
29. W. Xu, F. Lyu, Y. Bai, A. Gao, J. Feng, Z. Cai and Y. Yin, *Nano Energy*, 2018, **43**, 110-116.
30. X. Chen, Z. Yan, M. Yu, H. Sun, F. Liu, Q. Zhang, F. Cheng and J. Chen, *J. Mater. Chem. A*, 2019, **7**, 24868-24876.
31. Y. Wang, T. Zhou, K. Jiang, P. Da, Z. Peng, J. Tang, B. Kong, W. B. Cai, Z. Yang and G. Zheng, *Adv. Energy Mater.*, 2014, **4**, 1400696.
32. S. Mao, Z. Wen, T. Huang, Y. Hou and J. Chen, *Energy Environ. Sci.*, 2014, **7**, 609-616.
33. T. Shinagawa, A. T. Garcia-Esparza and K. Takanebe, *Sci. Rep.*, 2015, **5**, 13801.
34. J. Rossmeisl, Z. W. Qu, H. Zhu, G. J. Kroes and J. K. Nørskov, *J. Electroanal. Chem.*, 2007, **607**, 83-89.
35. I. C. Man, H.-Y. Su, F. Calle-Vallejo, H. A. Hansen, J. I. Martínez, N. G. Inoglu, J. Kitchin, T. F. Jaramillo, J. K. Nørskov and J. Rossmeisl, *ChemCatChem*, 2011, **3**, 1159-1165.
36. R. R. Rao, A. Bucci, S. Corby, B. Moss, C. Liang, A. Gopakumar, I. E. L. Stephens, J. Lloret-Fillol and J. R. Durrant, *ACS Catal.*, 2024, **14**, 11389-11399.
37. K. Iwase, I. Honma and T. Tomai, *ChemRxiv*, 2025, DOI: 10.26434/chemrxiv-2025-39618.
38. B. J. Kim, E. Fabbri, D. F. Abbott, X. Cheng, A. H. Clark, M. Nachtegaal, M. Borlaf, I. E. Castelli, T. Graule and T. J. Schmidt, *J. Am. Chem. Soc.*, 2019, **141**, 5231-5240.
39. E. Fabbri, M. Nachtegaal, T. Binninger, X. Cheng, B. J. Kim, J. Durst, F. Bozza, T. Graule, R. Schaublin, L. Wiles, M. Pertoso, N. Danilovic, K. E. Ayers and T. J. Schmidt, *Nat. Mater.*, 2017, **16**, 925-931.
40. D. Friebel, M. W. Louie, M. Bajdich, K. E. Sanwald, Y. Cai, A. M. Wise, M. J. Cheng, D. Sokaras, T. C. Weng, R. Alonso-Mori, R. C. Davis, J. R. Bargar, J. K. Nørskov, A. Nilsson and A. T. Bell, *J. Am. Chem. Soc.*, 2015, **137**, 1305-1313.
41. B. Sarac and A. Sezai Sarac, *ChemCatChem*, 2024, **16**.
42. H. Ding, H. Liu, W. Chu, C. Wu and Y. Xie, *Chem Rev*, 2021, **121**, 13174-13212.
43. M. S. Burke, L. J. Enman, A. S. Batchellor, S. Zou and S. W. Boettcher, *Chem. Mater.*, 2015, **27**, 7549-7558.



44. S. Samira, J. Hong, J. C. A. Camayang, K. Sun, A. S. Hoffman, S. R. Bare and E. Nikolla, *JACS Au*, 2021, **1**, 2224-2241.
45. C. W. Tung, Y. Y. Hsu, Y. P. Shen, Y. Zheng, T. S. Chan, H. S. Sheu, Y. C. Cheng and H. M. Chen, *Nat. Commun.*, 2015, **6**, 8106.
46. G. Ding, H. Lee, Z. Li, J. Du, L. Wang, D. Chen and L. Sun, *Adv. Energy Sustain. Res.*, 2022, **4**, 2200130.
47. W. Yan, Y. Mou, M. Li, K. Ma, Z. Xu, T. Lu, H. Du, C. Wang, H. Sun, L. Chen, Y. Tang, Y. Wang and G. Fu, *Adv. Mater.*, 2025, **37**, 2506936.
48. H. Zhang, H. Guo, F. Zhang, J. Zhang, Y. Cheng, Y. Ma, L. Ma and L. Qi, *Energy Environ. Sci.*, 2025, **18**, 6141-6153.
49. H. J. Niu, C. Huang, T. Sun, Z. Fang, X. Ke, R. Zhang, N. Ran, J. Wu, J. Liu and W. Zhou, *Angew. Chem. Int. Ed.*, 2024, **63**, e202401819.
50. K. Yassin, R. Attias, Y. Tsur and D. R. Dekel, *ACS Electrochemistry*, 2025, **1**, 655-666.
51. L. Zeng, Z. Zhao, Q. Huang, C. Zhou, W. Chen, K. Wang, M. Li, F. Lin, H. Luo, Y. Gu, L. Li, S. Zhang, F. Lv, G. Lu, M. Luo and S. Guo, *J. Am. Chem. Soc.*, 2023, **145**, 21432-21441.
52. Y. Zhang, Q. Wan, L. Huang, T. Jiang, S. Wu, D. Li, Y. Liu, H. Wu and F. Ren, *J. Mater. Chem. A*, 2025, **13**, 17384-17392.
53. L. Guo, Y. Huang, Y. Qin, B. Chen, C. Liu, H. Chen, J. Zhang, X. Zhang and Q. Wang, *Nanoscale*, 2025, **17**, 17312-17323.
54. B. Ravel and M. Newville, *J. Synchrotron Radiat.*, 2005, **12**, 537-541.
55. P. K. Gangadharan, H. Kuroki, S. Miyanishi, H. Okuyama and T. Yamaguchi, *ACS Appl. Energy Mater.*, 2025, **8**, 10637-10646.
56. S. Narayanaru, H. Kuroki, T. Tamaki, G. M. Anilkumar and T. Yamaguchi, *RSC Sustain.*, 2025, **3**, 1705-1713.
57. K. Nagasawa, T. Ishida, H. Kashiwagi, Y. Sano and S. Mitsushima, *Int. J. Hydrog. Energy*, 2021, **46**, 36619-36628.

View Article Online
DOI: 10.1039/D6TA00970K



View Article Online
DOI: 10.1039/D6TA00970K

The data supporting this article have been included as part of the Supplementary Information.

